photochem

MDPI

Article

Enhanced Photocatalytic Dehalogenation Performance of RuDoped In_2O_3 Nanoparticles Induced by Oxygen Vacancy

Jingjing Xiang [1,†], Jinting Shang [2,†] and Zhen Wan [1,*]

[1] Key Laboratory of Catalysis and Materials Science of the State Ethnic Affairs Commission and Ministry of Education, College of Resources and Environmental Science, South-Central Minzu University, Wuhan 430074, China; xiangjingjing1124@163.com

[2] Wuhan Institute of Biomedical Sciences, School of Medicine, Jianghan University, Wuhan 430056, China; shangjinting@jhun.edu.cn

* Correspondence: 2018030@scuec.edu.cn; Tel.: +86-27-67843990

† These authors contributed equally to this work.

Abstract: Due to its favorable excited-state physicochemical properties, indium oxide (In_2O_3) has widely captured attention as a potentially great photocatalyst. However, an inferior charge separation efficiency limits its application. Recently, an increasing amount of evidence has demonstrated that the construction of surface defects is an effective strategy to boost photocatalytic performances. In this work, a ruthenium (Ru) species was successfully introduced into the lattice of In_2O_3 nanoparticles through co-precipitation and thermal treatment. It was found that the content of surface oxygen vacancies was directly related to the amount of Ru^{3+} doping, which further determines the separation efficiency of photogenerated carriers. As a result, the 0.5% Ru-In_2O_3 samples enriched with oxygen vacancies exhibit dramatically enhanced photocatalytic dehalogenation performances of decabromodiphenyl ether and hexabromobenzene, about four times higher than that of the pure In_2O_3 nanoparticles. This study emphasized the significance of the surface defects of the photocatalyst and may provide a valuable strategy to prepare highly active photocatalysts for photocatalytic dehalogenation reactions.

Keywords: Ru−In_2O_3; oxygen vacancies; photocatalytic dehalogenation

check for updates

Citation: Xiang, J.; Shang, J.; Wan, Z. Enhanced Photocatalytic Dehalogenation Performance of RuDoped In_2O_3 Nanoparticles Induced by Oxygen Vacancy. *Photochem* **2023**, *3*, 360–372. https://doi.org/10.3390/photochem3030022

Academic Editors: Wanhong Ma, Chuanyi Wang and Mirela Petruta Suchea

Received: 28 May 2023
Revised: 21 July 2023
Accepted: 1 August 2023
Published: 1 September 2023

1. Introduction

Brominated flame retardants, such as decabromodiphenyl ether (Deca−BDE) and hexabromobenzene (HBB), are widely used in various industries to attain effective fire resistance for consumer products (e.g., textiles, electronics, etc.) [1,2]. Recently, an increasing amount of research has reported that these kinds of aryl halides, as a series of endocrine hormones, have high toxicity, environmental persistence and bioaccumulation potential, which might pose significant harm to humans and animals [3–8]. In order to control pollution due to brominated flame retardants, various technologies have been developed. Among them, photocatalysis, as one of the most promising green and renewable environmental treatment technologies, has proved to be effective in the removal of brominated flame retardants [9–11]. For instance, TiO_2 photocatalysis has been used in the degradation of polybrominated diphenyl ethers (PBDEs) in a series of liquid systems [12]. Zhang et al. found that the In_2O_3 nanospheres can be used as a visible-light responsive catalyst for the decomposition of gaseous aryl halides [13]. However, these reported catalysts have the common problem of low photocatalytic performances, which are mainly due to the low separation efficiency of photogenerated electron–hole pairs [14]. To solve this problem, many modification methods, such as facet engineering, novel metal deposition and the construction of heterojunctions, were studied. Guo et al. reported that Pd nanoclusters decorated with TiO_2 nanosheets were able to rapidly degrade 4-bromobiphenyl in 30 min

due to a strong chemical interaction and effective electron transfer [15]; Feng et al. confirmed that the exposed high-energy facets of Co_3O_4 nanosheets greatly promoted the separation efficiency of photogenerated electron–hole pairs and significantly enhanced the photocatalytic performances [16]; Liu et al. facilitated the charge separation at the TiO_2/Bi_2MoO_6 interface by fabricating heterojunctions [17].

Besides the above approaches, it has been reported that the construction of surface defects, such as oxygen or hydroxide defects, could also promote photocatalytic performance by improving the charge separation efficiency and adjusting the localized electronic states of semiconductors [18–22]. In this case, surface defects often serve as active sites for promoting the transfer of photogenerated electrons, both in the bulk phase and interface, thereby improving the separation efficiency of photogenerated carriers [23–25]. Among them, oxygen vacancies are one of the most common defects on a semiconductor's surface. For the semiconductor photocatalysts, one way to produce an oxygen-vacancy-rich surface is by adjusting the reductive preparation conditions. For example, Bi et al. synthesized defective $K_4Nb_6O_7$ nanosheets by introducing oxygen vacancies with the decomposition of KBH_4, which had a six-times higher hydrogen evolution rate than that of the $K_4Nb_6O_7$ samples without oxygen vacancies [26]; Yang et al. found that the oxygen vacancy content of the OV_H-TiO_2 obtained by reducing TiO_2 aggregates in a hydrogen atmosphere was much higher than that of the original TiO_2 samples [27]. As another method, ion doping is also an effective way to adjust the oxygen vacancy content. Moreover, a disordered surface caused by ion doping may intensify the localization of electrons, which is beneficial for transferring photogenerated electrons and lowering the activation energy of the reaction. In this case, Wang et al. prepared TiO_2 nanorods enriched with oxygen vacancies through a C-N-S three-doping method to enhance its visible photocatalytic activity [28]; Huang et al. used metallic Cu and Bi nanoparticles to co-modify the $BiVO_4$ to generate surface oxygen vacancies, which exhibited a higher absorption capacity for visible light and a superior charge separation efficiency compared to the original one [29]. In particular, it has been reported that Ru dopants were intentionally introduced into the In_2O_3 lattice as active sites, which not only narrow the bandgap energy but also cause the formation of oxygen vacancies, improving catalytic activity [30,31]. In addition, besides oxygen vacancy formation, the doping of Ru species could lead to an excellent hydrogen spillover effect, promoting hydrogen dissociation and adsorption, which is significant for the reduction reactions coupled with protons, such as the dehalogenation of brominated flame retardants [32].

In this work, we synthesized Ru−In_2O_3 nanoparticles with different oxygen vacancy contents by doping different amounts of Ru^{3+} in the lattice of In_2O_3. Characterization results indicate that the oxygen vacancy content of In_2O_3 is directly related to Ru doping, of which the 0.5% Ru−In_2O_3 sample had the highest oxygen vacancy content. The photocurrent, electrochemical impedance and surface photovoltage response results confirm that the 0.5% Ru−In_2O_3 sample had the highest separation efficiency of photogenerated electron and hole pairs, which is in accordance with the XPS results. We selected Deca−BDE and HBB as the model organic pollutants to evaluate the photocatalytic dehalogenation performances of the as-prepared Ru−In_2O_3 samples. Compared with other samples, 0.5% Ru−In_2O_3 nanoparticles exhibited superior photocatalytic dehalogenation activities for the removal of both Deca−BDE and HBB, which are closely related to its highest content of surface oxygen vacancies. Our results indicate that the increased oxygen vacancy content of photocatalysts caused by ion doping could effectively promote the removal efficiency of brominated flame retardants, which are persistently toxic in the environment.

2. Materials and Methods

2.1. Chemical Reagents

Indium nitrate hydrate ($In(NO_3)_3 \cdot H_2O$) and ruthenium chloride ($RuCl_3$) were obtained from Innochem Chemical Reagent Co. Ammonia solution (NH_4OH), ethyl alcohol and isopropyl alcohol were purchased from Sinopharm Chemical Reagent. Deionized water was obtained from Wahaha Group Co., Ltd (Hangzhou, China). Nafion was purchased

from Sigma-Aldrich (St Louis, MO, USA). All the other chemical reagents were purchased from J&K Chemicals Co (Beijing, China). All chemicals used in this work were purchased in analytical grade and used without any purification.

2.2. Synthesis of Ru−In_2O_3 Nanoparticles

Ru−In_2O_3 nanoparticles were synthesized following a modified version of a previously published procedure [23]. All chemicals were used as received without any further purification. In a typical synthesis, 1.8 mmol of the $In(NO_3)_3 \cdot H_2O$ was dissolved in a mixed solution containing 6 mL of anhydrous ethanol and 2 mL of deionized water to obtain solution A. Solution B was prepared by adding 2.5 mL of ammonia solution (27%) into 7.5 mL of anhydrous ethanol. Then, the above solution A and solution B were rapidly mixed together to form a white suspension, which was immediately transferred to a pre-heated oil bath at 80 °C and stirred for 10 min. The resulting suspension was then removed from the oil bath and allowed to settle and cool to room temperature before being centrifuged, washed three times with deionized water and ethanol, respectively and dried in a freeze dryer for 10 h. The dried precursor was collected, ground, and then calcined in a muffle furnace at 250 °C in air for 3 h to obtain the sample labeled as 0% Ru−In_2O_3. $RuCl_3$ was added into the solution A under different Ru/In molar ratios (0.1%, 0.5% and 1%) with the other steps remaining unchanged to obtain the samples labeled as 0.1% Ru−In_2O_3, 0.5% Ru−In_2O_3 and 1% Ru−In_2O_3, respectively.

2.3. Characterization

The structure and phase of the as-prepared samples were determined by X-ray diffraction (XRD) analysis on a D8 ADVANCE diffractometer with Cu Kα radiation. The Cu target wavelength was 0.154056 Å, and the slit width was 5 nm. The samples were pressed into a pellet and scanned in the range of a 10°–80° diffraction angle with a step size of 0.02 °/step and a scan speed of 0.1 s/step. The chemical compositions were tested by X-ray photoelectron spectroscopy (Thermo Electron Corporation, Waltham, MA. USA) with Al Kα radiation. The samples were uniformly applied to a double–sided adhesive surface for testing, and the scanning range was -9 eV–1551 eV with dwell time of 58 s and pass energy of 30 eV. All the binding energies were calibrated by carbon (C1s 285.0 eV). The morphology and size of the as-prepared samples were examined by field emission scanning electron microscopy (FESEM, S-4800). Photocurrent and electrochemical impedance spectroscopy (EIS) in Na_2SO_4 (0.5 M) aqueous solution were acquired on a CHI660 electrochemical workstation with a standard three-electrode cell, where 75 mg of the as-prepared catalyst sample powders were sonicated in a mixture of 1.5 mL isopropanol and 20 μL Nafion solution for 30 min. Then, 20 μL of the suspensions were dripped onto a 1 × 1 cm^2 size FTO conductive glass as the working electrode, a Pt electrode as auxiliary electrode, and a standard calomel electrode as reference. Photocurrent measurement used a 300 W xenon lamp as the light source, and the frequency in the electrochemical impedance spectroscopy test ranged from 100 kHz to 0.1 Hz. The surface photovoltage spectroscopy (SPS) measurements were performed according to the previous reports [33,34].

2.4. Photocatalytic Dehalogenation Reactions

Deca−BDE was dissolved in a tetrahydrofuran solvent to prepare a stock solution with a concentration of 10^{-3} mol/L. Prior to the experiments, the stock solution was diluted 100 times to a concentration of 10^{-5} mol/L using methanol as the solvent. The photocatalytic reaction was carried out in a freshly prepared 20 mL Deca−BDE solution with the addition of 15 mg of as-prepared photocatalysts in a Pyrex vessel. The vessel was sealed with a rubber stopper under an argon atmosphere. Before irradiation, the suspension was firstly magnetically stirred for 30 min in darkness to achieve the adsorption–desorption equilibrium, followed by purging with argon for 40 min to remove air. The suspension was then irradiated at constant temperature (25 °C) using cooling circulation water. A 300 W xenon lamp (CEL-HXF300, Beijing China Education Au-light Co., Ltd.) with a 400 nm

cutoff filter served as the light source. During the photocatalytic reaction, 1 mL of the suspension was sampled and centrifuged at predetermined time intervals. The supernatant was filtered through a 0.22 μm membrane and then analyzed using high-performance liquid chromatography (Thermo scientific Ultimate 3000 HPLC) equipped with a diode array detector and SB−C18 chromatographic column (4.6 × 150 mm). Pure methanol served as the mobile phase at a flow rate of 1.0 mL/min, while the detector wavelength was set at 240 nm. The photocatalytic degradation of HBB was carried out under similar experimental conditions as that of Deca−BDE, except for the quantity of the photocatalysts (30 mg). Cyclic tests were carried out under identical experimental conditions as those employed for the Deca−BDE degradation. Before each cycle, the recovered samples, including the filtered particles on the membrane and the remaining precipitates in the vessel, were collected and dried using a freeze dryer for 6 h.

3. Results and Discussion

3.1. Characterizations of Ru−In_2O_3 Nanoparticles

XRD, SEM and TEM/HRTEM measurements were carried out to study the structure and morphology of the as-prepared Ru−In_2O_3 samples. Figure 1 illustrates the XRD patterns of different Ru−In_2O_3 samples. From the figure, it can be observed that all the samples retained the characteristic cubic structure of In_2O_3 and are in good agreement with the standard pattern (JCPDS Card no. 44-1087), which indicates that well-crystallized single-phase In_2O_3 had been successfully synthesized under the current experimental conditions. The diffraction peaks at 2θ = 21.5°, 30.5°, 35.4°, 37.6°, 41.8°, 45.6°, 51.0°, 55.9° and 60.6° are assigned to the (211), (222), (400), (411), (332), (431), (440), (611) and (622) planes of cubic In_2O_3, respectively. With increasing the Ru-doping content in the as-prepared Ru−In_2O_3 samples, there were no significant changes observed in terms of intensity or the position of diffraction peaks, indicating that Ru doping did not alter the crystal structure of In_2O_3 components. The strong and sharp diffraction peaks imply good crystallinity of the samples. No diffraction peaks of Ru components or other impurities were observed in any of the samples, possibly because the doped Ru components were too little to reach the detection limit. Additionally, the Scherrer equation was employed to calculate the crystallite sizes of different Ru−In_2O_3 samples. The calculated results for 0% Ru−In_2O_3, 0.1% Ru−In_2O_3, 0.5% Ru−In_2O_3 and 1% Ru−In_2O_3 samples are 7.89, 8.60, 8.24 and 8.34 nm, respectively. Meanwhile, the morphology and size of the as-prepared Ru−In_2O_3 samples were also characterized by the SEM and TEM/HRTEM images presented in Figures 2 and 3. SEM images in Figure 2a and Figure S3 reveal that the 0% Ru−In_2O_3 samples are irregular agglomerates with spherical nanoparticles less than 10 nm in size, which is in accordance with the XRD results. From the SEM and TEM images in Figure 2b, Figure S4 and Figure 3a, the 0.5% Ru−In_2O_3 samples exhibit no significant change in shape and size compared to those of the 0% Ru−In_2O_3 samples. Moreover, Figure 3b contains a HRTEM image displaying clear crystal lattice fringes with a spacing of 0.291 nm attributed to the (222) plane of cubic In_2O_3 (JCPDS Card no.44-1087), which is consistent with our XRD findings.

The optical properties of the as-prepared samples were studied using UV-visible diffuse reflectance spectroscopy. As shown in Figure 4a, compared to the pure In_2O_3 samples, the absorption band edges of the Ru-doped In_2O_3 samples have undergone a significant red shift, which gradually increased with the increase of Ru content. As shown in Figure 4b, the optical band gap energy (E_g) of the as-prepared Ru−In_2O_3 samples was calculated by Tauc plot according to the results of the UV diffuse reflectance spectra. The calculation formula is as follows [35,36],

$$(\alpha hv) = A(hv - E_g)^{n/2}$$
$$hv = 1240/\lambda$$

where α represents the absorption coefficient, h is the Planck constant, v is the vibration frequency of light, A is a proportionality constant, and the exponent n is related to the semiconductor type [37]. From Figure 4b, it was calculated that the band gaps of 0%

Ru−In_2O_3, 0.1% Ru−In_2O_3, 0.5% Ru−In_2O_3 and 1% Ru−In_2O_3 were 2.92 eV, 2.62 eV, 2.21 eV and 2.27 eV, respectively. The doping of Ru evidently enhanced absorption in the visible light region.

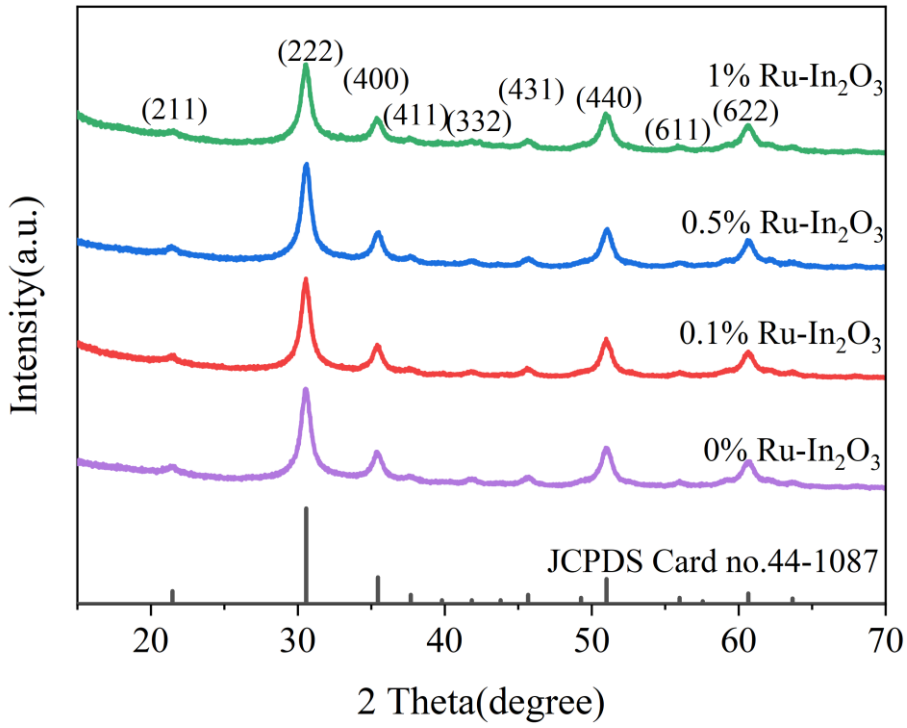

Figure 1. XRD patterns of the different as-prepared Ru−In_2O_3 samples.

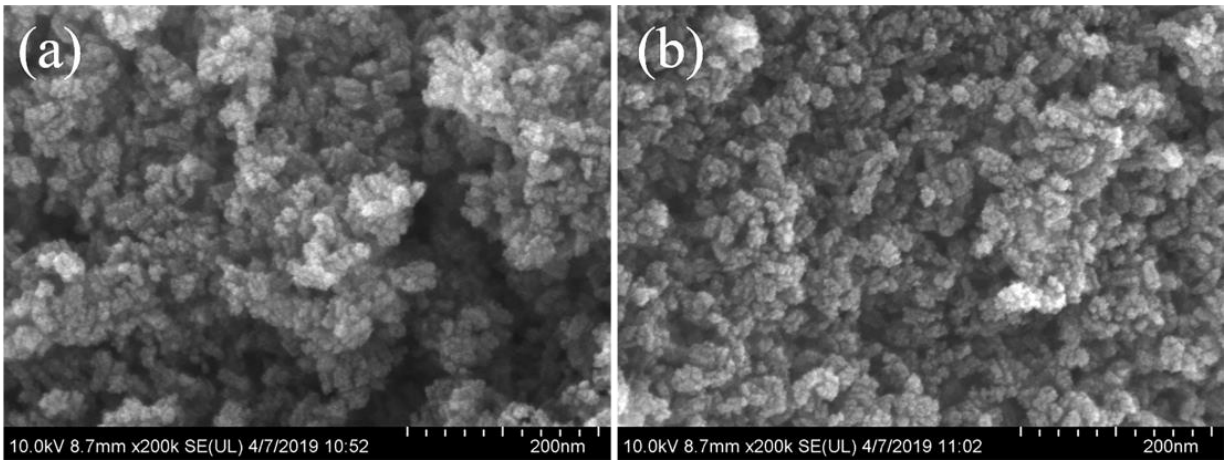

Figure 2. SEM images of the (**a**) 0% Ru−In_2O_3 and (**b**) 0.5% Ru−In_2O_3 samples.

XPS measurements were performed to further study the surface element composition, chemical state and the amount of oxygen vacancy. Figure 5a shows the survey XPS spectrum of the 0.5% Ru−In_2O_3 samples, in which the binding energy peaks of In 4d, In 4s, Ru 3d, In 3d, O 1s, In 3p and In 3s were detected, indicating the existence of In, O and Ru elements in the Ru−In_2O_3 samples. Especially, in Figure 5b, the high-resolution XPS spectrum of Ru 3d located at 284.3 eV indicates that Ru^{3+} has been successfully doped into the In_2O_3 lattices. As shown in Figure 5c, the peaks at 444.4 and 452.0 eV are attributed to the binding energies of the In $3d_{5/2}$ and In $3d_{3/2}$ levels, respectively, which correspond to the In^{3+} in the In_2O_3 lattices according to previous reports [38,39]. From the O 1s region in Figure 5d, the O 1s binding energy peak at around 529.7 eV is attributed to the lattice oxygen of In_2O_3

components, while the appearance of shoulder peaks with higher binding energies can be attributed to the combination of chemisorbed oxygen and surface hydroxyl groups, which can be divided into peaks at around 530.9 eV and 532.0 eV, respectively [38]. It is reported that the chemisorbed oxygen of In_2O_3 is caused by oxygen vacancy [39]. Hence, from the O 1s core-level XPS spectra in Figure 6, we used the ratios of peaks around at 530.9 eV to quantify the surface oxygen vacancy contents of the as-prepared Ru−In_2O_3 samples and the results were listed in Table 1. From Table 1, the O_L, O_V and O_H represent the oxygen atoms from the lattice, chemisorbed oxygen and surface hydroxyl groups of different Ru−In_2O_3 samples, respectively. Among them, for the 0.5% Ru−In_2O_3 samples the ratio of oxygen vacancy to all oxygen species was 44.3%, obviously higher than that of In_2O_3 doped with 0%, 0.1% and 1% Ru (20.6%, 22.6% and 22.2%, respectively), which could directly lead to its superior photocatalytic behaviors as discussed below.

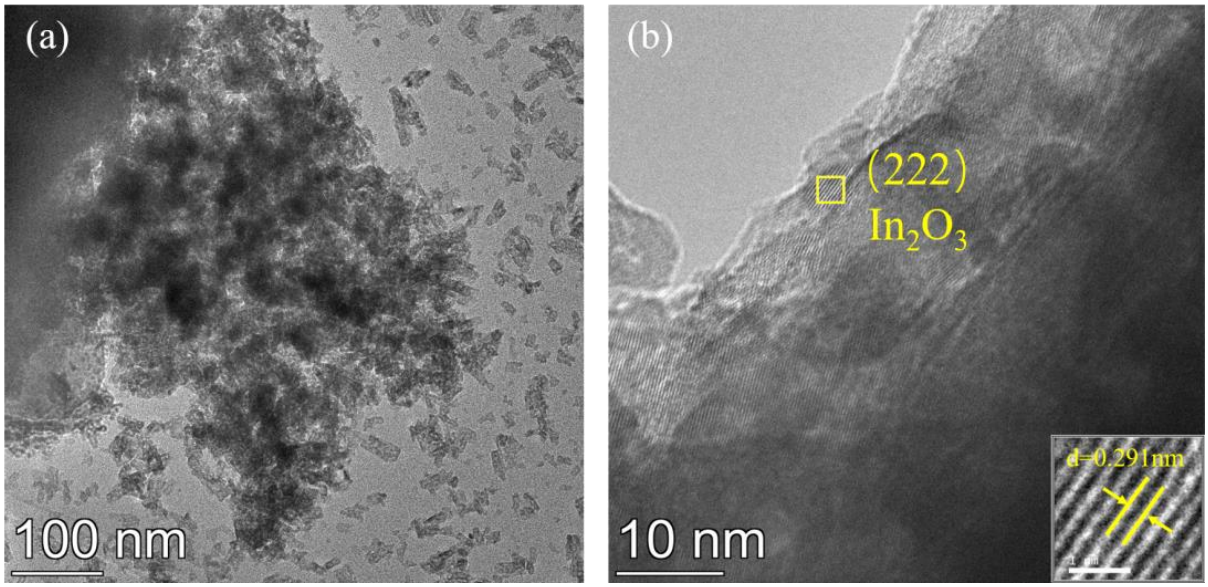

Figure 3. TEM (**a**) and HRTEM (**b**) images of the 0.5% Ru−In_2O_3 samples.

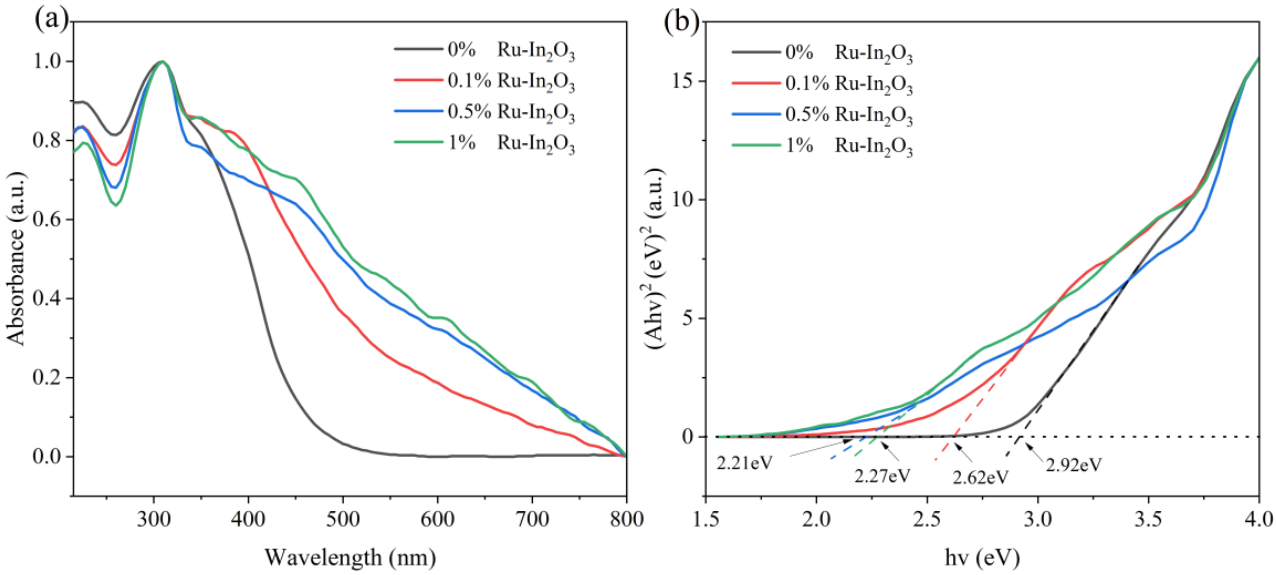

Figure 4. (**a**) UV-Vis diffuse reflection spectra of the different as-prepared Ru−In_2O_3 samples. (**b**) Plot of the $(Ahv)^2$ versus hv for the different as-prepared Ru−In_2O_3 samples.

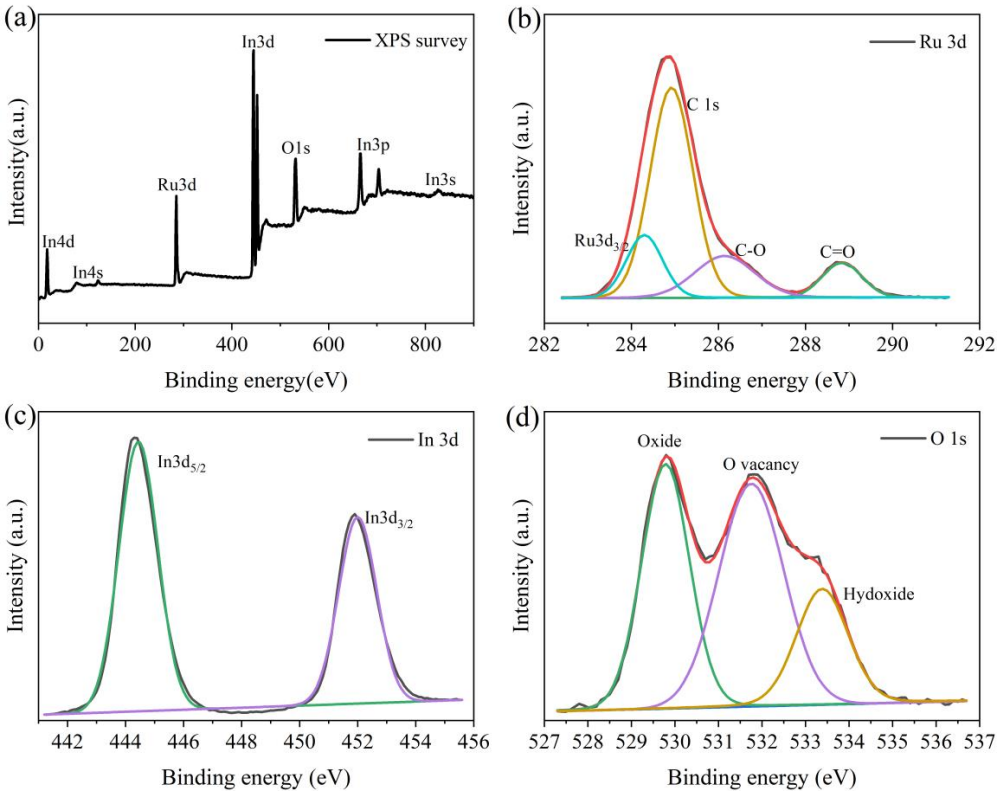

Figure 5. (**a**) Survey XPS spectrum and (**b**–**d**) high-resolution XPS spectra of Ru 3d, In 3d regions, respectively, of the 0.5% Ru−In_2O_3 samples.

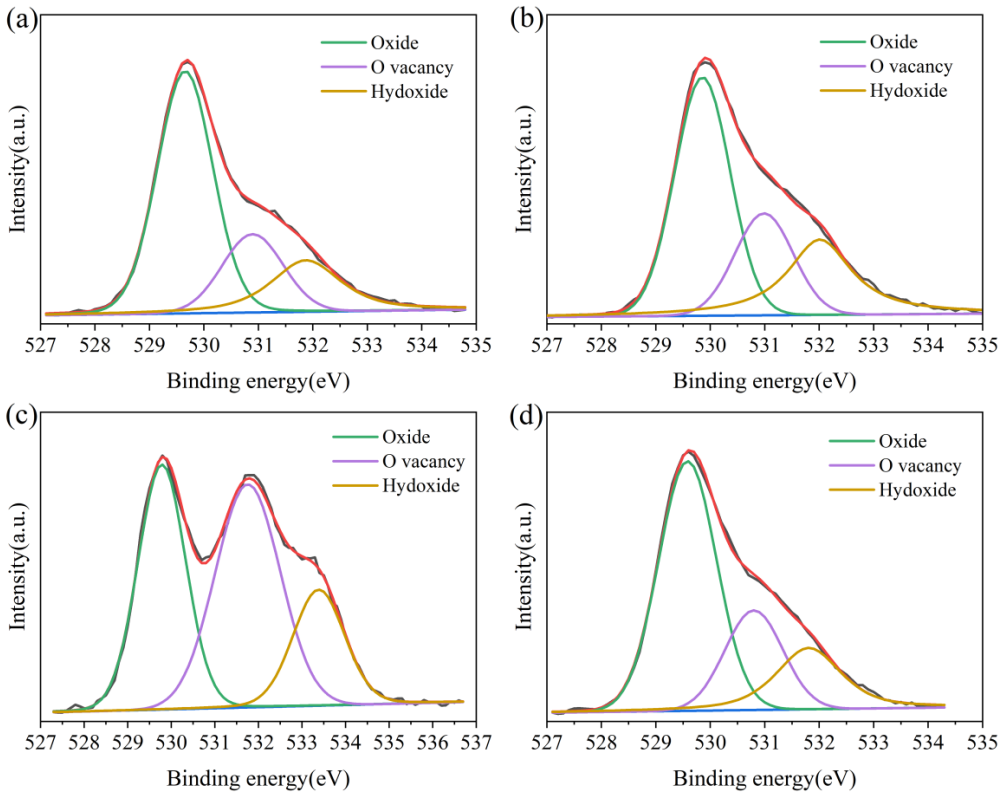

Figure 6. XPS O 1s core-level spectra of different Ru−In_2O_3 samples: (**a**) 0% Ru−In_2O_3, (**b**) 0.1% Ru−In_2O_3, (**c**) 0.5% Ru−In_2O_3, (**d**) 1% Ru−In_2O_3.

Table 1. Atom ratio of the O_L, O_V and O_H for different Ru−In_2O_3 samples.

Sample	Atom Ratio of O_L (%)	Atom Ratio of O_V (%)	Atom Ratio of O_H (%)	Atom Ratio of Ru (%)
0% Ru−In_2O_3	59.3	20.6	20.1	0
0.1% Ru−In_2O_3	50.4	22.6	27.0	0.1
0.5% Ru−In_2O_3	36.5	44.2	19.3	0.5
1% Ru−In_2O_3	56.5	22.2	21.3	1.0

Photocurrent response, electrochemical impedance spectroscopy (EIS) and surface photovoltage response (SPS) measurements were used to investigate the delocalization and separation efficiency of photogenerated carriers. As shown in Figure 7a, the photocurrent response of 0.5% Ru−In_2O_3 under visible light irradiation was significantly higher than that of the 0% Ru−In_2O_3, 0.1% Ru−In_2O_3 and 1% Ru−In_2O_3, indicating the photogenerated carriers of 0.5% Ru−In_2O_3 have the highest separation efficiency. From Figure 7b, the EIS plot of the 0.5% Ru−In_2O_3 samples exhibits a smaller arc radius than that of other Ru−In_2O_3 samples, indicating an improvement of migration and delocalization of photogenerated carriers. As shown in Figure 7c, the SPS response curves of all the Ru−In_2O_3 samples display a broad peak from 300 to 450 nm. Similarly, the SPS response of the 0.5% Ru−In_2O_3 samples is much more intense in comparison with that of other Ru−In_2O_3 samples. All the above mentioned results prove that the 0.5% Ru−In_2O_3 sample exhibits an enhanced delocalization and separation efficiency of photogenerated carriers, which is closely related to its higher surface oxygen vacancy content.

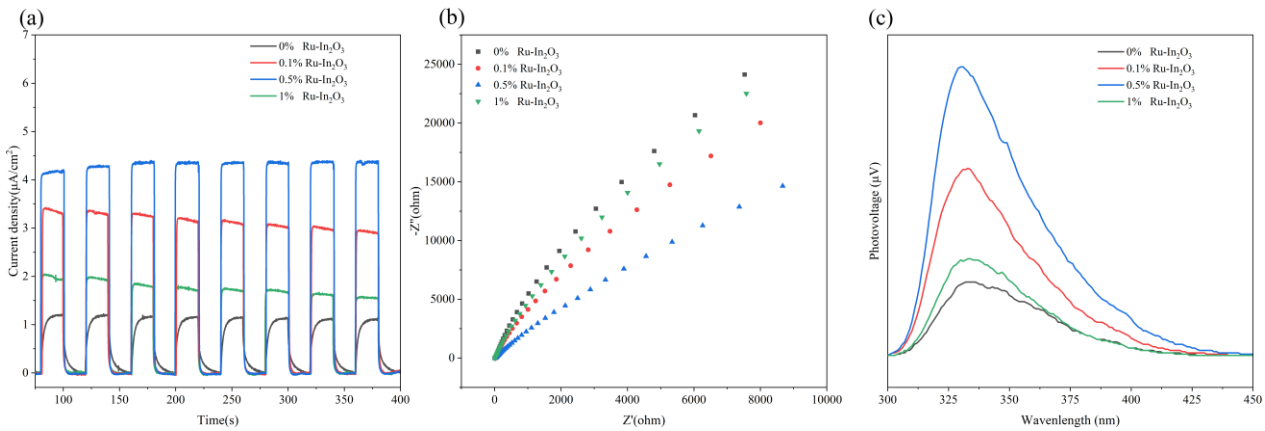

Figure 7. (**a**) Photocurrent responses, (**b**) electrochemical impedance spectra and (**c**) surface photovoltage responses of the different as-prepared Ru−In_2O_3 samples.

3.2. Photocatalytic Activity

Two typical brominated flame retardants, which are toxic substances in the environment (Deca−BDE and HBB), were used to evaluate the photocatalytic performance of Ru−In_2O_3 samples under visible light and Ar conditions. Figure 8, Figures S5 and S6 show the time profiles and corresponding kinetic values of different Ru−In_2O_3 samples for the photocatalytic dehalogenation of Deca−BDE and HBB, respectively. As shown in Figure 8a, the photolysis of the Deca−BDE was negligible under visible light irradiation while the removal efficiency of Deca−BDE by 0% Ru−In_2O_3 samples was only 76.4% within 30 min. With the doping of Ru, the removal efficiency increased and the removal efficiency of 0.5% Ru−In_2O_3 for Deca−BDE reached 96.3% within 30 min due to the promotion of surface oxygen vacancy content. However, excessive Ru doping (1%) caused the sliding of surface oxygen vacancy and thus resulted in the decrease of removal efficiency of Deca−BDE to 82.4% under the same experiment conditions. Figure 8c shows the corresponding apparent rate constant (K) of different Ru−In_2O_3 samples for the photocatalytic dehalogenation of Deca−BDE. From the figure, the K values of 0-1% Ru−In_2O_3 samples are 0.05457, 0.06833,

0.13067 and 0.05856 min^{-1}, respectively. The photocatalytic dehalogenation efficiency of 0.5% Ru−In_2O_3 samples is about 2.4 times higher than that of the 0% Ru−In_2O_3 samples.

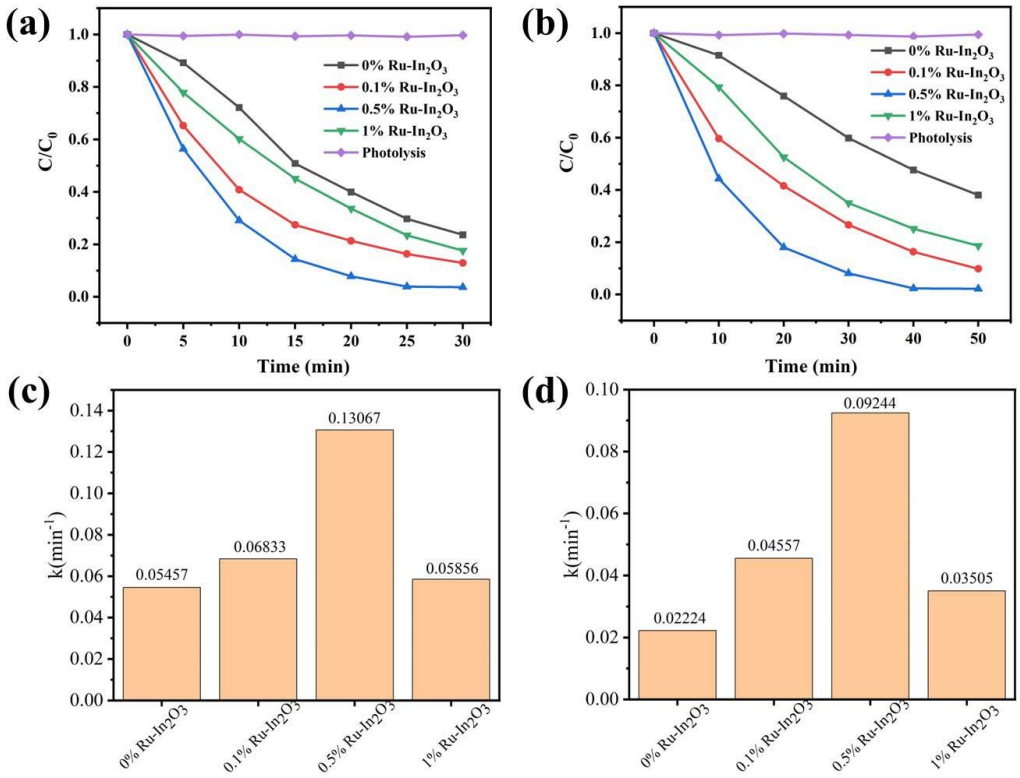

Figure 8. (**a**) Photocatalytic performances for the degradation of Deca−BDE (**a**) and HBB (**b**) over the different Ru−In_2O_3 samples and (**c**,**d**) corresponding kinetic studies.

Meanwhile, the photocatalytic dehalogenation of HBB exhibited a similar tendency. As shown in Figure 8b, Within 50 min, the removal efficiency of HBB by 0.5% Ru−In_2O_3 samples reached a maximum of 97.8%. Moreover, the calculated K values in Figure 8d for 0-1% Ru−In_2O_3 samples are 0.02224, 0.04557, 0.09244 and 0.03505 min^{-1}, respectively. For the dehalogenation of HBB, the removal efficiency of 0.5% Ru−In_2O_3 samples is about four times higher than that of the 0% Ru−In_2O_3 samples. These results are consistent with the above XPS results, indicating that the surface oxygen vacancy content is directly related to the separation efficiency of photogenerated carriers and thus determines the photocatalytic activities of the Ru−In_2O_3 samples. In addition, we have compared the photocatalytic performances of Deca−BDE over Ru−In_2O_3 samples with seven other kinds of photocatalysts [40–42]. As shown in Table S1, the as-prepared Ru−In_2O_3 samples exhibited superior photocatalytic dehalogenation performances compared to other photocatalysts, indicating that the increase of oxygen vacancy content is an effective way to improve photocatalytic performances in dehalogenation reactions. IC (ion chromatography) was used to study the transformation products during photocatalytic degradation. As shown in Figure S1, the formation of the bromide ion in the dehalogenation of Deca−BDE was much higher than the conversion of Deca−BDE, which might be due to the further degradation of Nona−BDE to Octa−BDE. Similar results could also be seen in the dehalogenation of HBB (Figure S2), in which tetrabromo-benzene might be formed during the photocatalytic reactions.

Furthermore, we tested the stability of 0.5% Ru−In_2O_3 samples through cyclic experiments for the degradation of Deca−BDE. As shown in Figure 9, the photocatalytic dehalogenation efficiency of the as-prepared Ru−In_2O_3 samples exhibits a gradual decline after five cycles, decreasing only from 97.7% to 91.3% after five cycles, indicating the remarkable reusability of the as-prepared 0.5% Ru−In_2O_3 samples in this reaction system. Moreover, we used XRD and FTIR to study the phase structure of the Ru−In_2O_3 samples

after the reusability tests. In Figure 10a,b, no significant deviations can be observed in both XRD patterns and FTIR spectra of the 0.5% Ru−In_2O_3 samples before and after undergoing cyclic tests, thus confirming their exceptional stability.

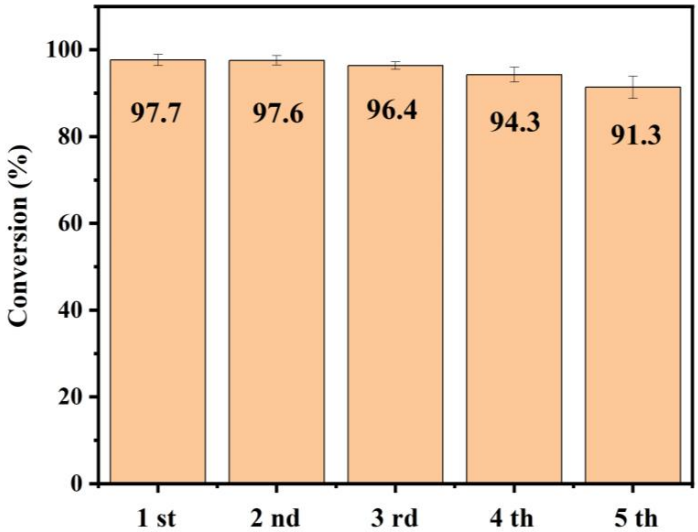

Figure 9. Cyclic tests over the 0.5% Ru−In_2O_3 samples.

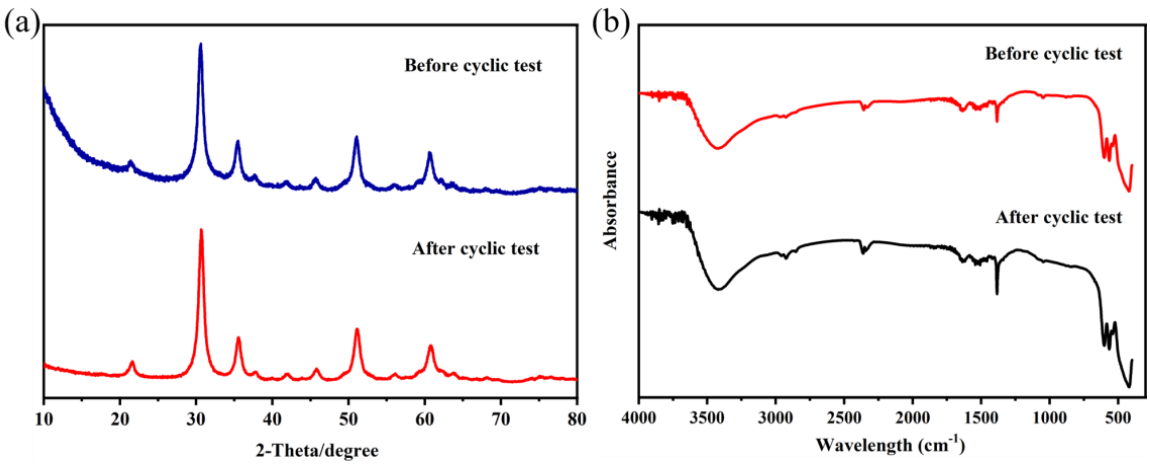

Figure 10. XRD patterns (**a**) and FTIR spectra (**b**) of the 0.5% Ru−In_2O_3 samples before and after the cyclic tests.

4. Conclusions

In summary, In_2O_3 nanoparticles with varying oxygen vacancy contents were created by doping Ru through co-precipitation and subsequent thermal treatment. Through comprehensive characterizations and measurements, we demonstrated the effective modulation of oxygen vacancy content in the Ru−In_2O_3 samples via Ru doping. Meanwhile, the photocurrent, electrochemical impedance spectroscopy and surface photovoltage response measurements reveal that the increased oxygen vacancy content could effectively promote the separation efficiency of photogenerated electrons and holes, ultimately leading to improved photocatalytic performances of the as-prepared Ru−In_2O_3 samples. As a result, the 0.5% Ru−In_2O_3 enriched with oxygen vacancy exhibits dramatically enhanced photocatalytic dehalogenation performances of decabromodiphenyl ether and hexabromobenzene, approximately four times higher than that of the 0% Ru−In_2O_3 nanoparticles. This study emphasized the significance of the surface defects of the photocatalyst and may provide a valuable strategy to prepare highly active photocatalysts for brominated flame retardant removal.

Supplementary Materials: The following supporting information can be downloaded at: https://www.mdpi.com/article/10.3390/photochem3030022/s1, Figure S1: The formation of bromide ion in the photocatalytic dehalogenation of Deca–BDE over the 0.5% Ru−In_2O_3 samples; Figure S2: The formation of bromide ion in the photocatalytic dehalogenation of Deca–BDE over the 0.5% Ru−In_2O_3 samples; Figure S3: SEM image of the 0% Ru−In_2O_3 samples; Figure S4: SEM image of the 0.5% Ru−In_2O_3 samples; Figure S5: Kinetic studies for the degradation of Deca–BDE over the different Ru−In_2O_3 samples; Figure S6: Kinetic studies for the degradation of HBB over the different Ru−In_2O_3 samples; Table S1: The comparison of the photocatalytic performances with other studies [40–42].

Author Contributions: Conceptualization, J.X. and Z.W.; methodology, J.X., J.S. and Z.W.; investigation, J.X., J.S. and Z.W.; writing—original draft, J.X. and Z.W.; supervision, J.S. and Z.W.; writing—review and editing, Z.W. All authors have read and agreed to the published version of the manuscript.

Funding: This research was funded by the National Natural Science Foundation of China (Grant No. 21906184, 22006056) and the Fundamental Research Funds for the Central Universities, South-Central University for Nationalities (CZQ23008).

Data Availability Statement: The datasets generated during and/or analyzed during the current study are available from the corresponding author on reasonable request.

Acknowledgments: This work was financially supported by the College of Resources and Environmental Science of South-Central Minzu University.

Conflicts of Interest: All authors certify that the submission is original work and is not under review at any other publication. The authors declare no conflict of interest.

References

1. De-Wit, C.A. An Overview of Brominated Flame Retardants in the Environment. *Chemosphere* **2002**, *46*, 583–624. [CrossRef] [PubMed]
2. Wemken, N.; Drage, D.S.; Abdallah, M.A.; Harrad, S.; Coggins, M.A. Concentrations of Brominated Flame Retardants in Indoor Air and Dust from Ireland Reveal Elevated Exposure to Decabromodiphenyl Ethane. *Environ. Sci. Technol.* **2019**, *53*, 9826–9836. [CrossRef] [PubMed]
3. Hites, R.A. Polybrominated Diphenyl Ethers in the Environment and in People: A Meta-Analysis of Concentrations. *Environ. Sci. Technol.* **2004**, *38*, 945–956. [CrossRef]
4. Guo, S.; Zhu, L.; Majima, T.; Lei, M.; Tang, H. Reductive Debromination of Polybrominated Diphenyl Ethers: Dependence on Br Number of the Br-Rich Phenyl Ring. *Environ. Sci. Technol.* **2019**, *53*, 4433–4439. [CrossRef] [PubMed]
5. Yu, L.; Han, Z.; Liu, C. A Review on the Effects of PBDEs on Thyroid and Reproduction Systems in Fish. *Gen. Comp. Endocrinol.* **2015**, *219*, 64–73. [CrossRef] [PubMed]
6. Burreau, S.; Zebuhr, Y.; Broman, D.; Ishaq, R. Biomagnification of Polychlorinated Biphenyls (PCBs) and Polybrominated Diphenyl Ethers (PBDEs) Studied in Pike (*Esox lucius*), Perch (*Perca fluviatilis*) and Roach (*Rutilus rutilus*) from the Baltic Sea. *Chemosphere* **2004**, *55*, 1043–1052. [CrossRef] [PubMed]
7. Abbasi, G.; Li, L.; Breivik, K. Global Historical Stocks and Emissions of PBDEs. *Environ. Sci. Technol.* **2019**, *53*, 6330–6340. [CrossRef]
8. Zhou, C.; Pagano, J.; McGoldrick, D.J.; Chen, D.; Crimmins, B.S.; Hopke, P.K.; Milligan, M.S.; Murphy, E.W.; Holsen, T.M. Legacy Polybrominated Diphenyl Ethers (PBDEs) Trends in Top Predator Fish of the Laurentian Great Lakes (GL) from 1979 to 2016: Will Concentrations Continue to Decrease? *Environ. Sci. Technol.* **2019**, *53*, 6650–6659. [CrossRef]
9. Singh, A.R.; Dhumal, P.S.; Bhakare, M.A.; Lokhande, K.D.; Bondarde, M.P.; Some, S. In-situ Synthesis of Metal Oxide and Polymer Decorated Activated Carbon-Based Photocatalyst for Organic Pollutants Degradation. *Sep. Purif. Technol.* **2022**, *286*, 120380. [CrossRef]
10. Samanta, A.; Goswami, M.N.; Mahapatra, P.K. Fe-Doped ZnO Nanoparticles as Novel Photonic and Multiferroic Semiconductor. *Mater. Chem. Phys.* **2020**, *240*, 122180. [CrossRef]
11. Sun, C.; Zhao, D.; Chen, C.; Ma, W.; Zhao, J. TiO_2-Mediated Photocatalytic Debromination of Decabromodiphenyl Ether: Kinetics and Intermediates. *Environ. Sci. Technol.* **2009**, *43*, 157–162. [CrossRef] [PubMed]
12. Santos, M.S.F.; Alves, A.; Madeira, L.M. Chemical and Photochemical Degradation of Polybrominated Diphenyl Ethers in Liquid Systems—A Review. *Water Res.* **2016**, *88*, 39–59. [CrossRef] [PubMed]
13. Zhang, F.; Li, X.; Zhao, Q.; Chen, G.; Zhang, Q. High-Performance In_2O_3@Pani Core@Shell Architectures with Ultralong Charge Carriers Lifetime for Photocatalytic Degradation of Gaseous 1,2-Dichlorobenzene. *Appl. Catal. B Environ.* **2020**, *263*, 118278. [CrossRef]
14. Lei, M.; Wang, N.; Zhu, L.; Xie, C.; Tang, H. A Peculiar Mechanism for the Photocatalytic Reduction of Decabromodiphenyl Ether over Reduced Graphene Oxide–TiO_2 Photocatalyst. *Chem. Eng. J.* **2014**, *241*, 207–215. [CrossRef]

15. Guo, W.; Zou, J.; Guo, B.; Xiong, J.; Liu, C.; Xie, Z.; Wu, L. Pd Nanoclusters/TiO_2(B) Nanosheets with Surface Defects Toward Rapid Photocatalytic Dehalogenation of Polyhalogenated Biphenyls Under Visible Light. *Appl. Catal. B Environ.* **2020**, *277*, 119255. [CrossRef]
16. Feng, Z.; Zhu, X.; Yang, J.; Zhong, K.; Jiang, Z.; Yu, Q.; Song, Y.; Hua, Y.; Li, H.; Xu, H. Inherent Facet-Dominant Effect for Cobalt Oxide Nanosheets to Enhance Photocatalytic CO_2 Reduction. *Appl. Surf. Sci.* **2022**, *578*, 151848. [CrossRef]
17. Liu, Z.; Tian, J.; Zeng, D.; Yu, C.; Huang, W.; Yang, K.; Liu, X.; Liu, H. Binary-Phase TiO_2 Modified Bi_2MoO_6 Crystal for Effective Removal of Antibiotics under Visible Light Illumination. *Mater. Res. Bull.* **2019**, *112*, 336–345. [CrossRef]
18. Lai, Y.; Meng, M.; Yu, Y.; Wang, X.; Ding, T. Photoluminescence and Photocatalysis of the Flower-Like Nano-ZnO Photocatalysts Prepared by a Facile Hydrothermal Method with or without Ultrasonic Assistance. *Appl. Catal. B Environ.* **2011**, *105*, 335–345. [CrossRef]
19. Chen, S.; Wang, H.; Kang, Z.; Jin, S.; Zhang, X.; Zheng, X.; Qi, Z.; Zhu, J.; Pan, B.; Xie, Y. Oxygen Vacancy Associated Single-Electron Transfer for Photofixation of CO_2 to Long-Chain Chemicals. *Nat. Commun.* **2019**, *10*, 788. [CrossRef]
20. Lei, F.; Sun, Y.; Liu, K.; Gao, S.; Liang, L.; Pan, B.; Xie, Y. Oxygen Vacancies Confined in Ultrathin Indium Oxide Porous Sheets for Promoted Visible-Light Water Splitting. *J. Am. Chem. Soc.* **2014**, *136*, 6826–6829. [CrossRef]
21. Raizada, P.; Soni, V.; Kumar, A.; Singh, P.; Parwaz Khan, A.A.; Asiri, A.M.; Thakur, V.K.; Nguyen, V.-H. Surface Defect Engineering of Metal Oxides Photocatalyst for Energy Application and Water Treatment. *J. Mater.* **2021**, *7*, 388–418. [CrossRef]
22. Ni, M.; Zhu, Y.; Guo, C.; Chen, D.-L.; Ning, J.; Zhong, Y.; Hu, Y. Efficient Visible-Light-Driven CO_2 Methanation with Self-Regenerated Oxygen Vacancies in Co_3O_4/$NiCo_2O_4$ Hetero-Nanocages: Vacancy-Mediated Selective Photocatalysis. *ACS Catal.* **2023**, *13*, 2502–2512. [CrossRef]
23. Hoch, L.B.; He, L.; Qiao, Q.; Liao, K.; Reyes, L.M.; Zhu, Y.; Ozin, G.A. Effect of Precursor Selection on the Photocatalytic Performance of Indium Oxide Nanomaterials for Gas-Phase CO_2 Reduction. *Chem. Mater.* **2016**, *28*, 4160–4168. [CrossRef]
24. Ran, M.; Wang, H.; Cui, W.; Li, J.; Chen, P.; Sun, Y.; Sheng, J.; Zhou, Y.; Zhang, Y.; Dong, F. Light-Induced Generation and Regeneration of Oxygen Vacancies in $BiSbO_4$ for Sustainable Visible Light Photocatalysis. *ACS Appl. Mater. Interfaces* **2019**, *11*, 47984–47991. [CrossRef]
25. Geng, Z.; Kong, X.; Chen, W.; Su, H.; Liu, Y.; Cai, F.; Wang, G.; Zeng, J. Oxygen Vacancies in ZnO Nanosheets Enhance CO_2 Electrochemical Reduction to CO. *Angew. Chem. Int. Ed.* **2018**, *57*, 6054–6059. [CrossRef]
26. Bi, W.; Ye, C.; Xiao, C.; Tong, W.; Zhang, X.; Shao, W.; Xie, Y. Spatial Location Engineering of Oxygen Vacancies for Optimized Photocatalytic H_2 Evolution Activity. *Small* **2014**, *10*, 2820–2825. [CrossRef] [PubMed]
27. Yang, Y.; Yin, L.-C.; Gong, Y.; Niu, P.; Wang, J.-Q.; Gu, L.; Chen, X.; Liu, G.; Wang, L.; Cheng, H.-M. An Unusual Strong Visible-Light Absorption Band in Red Anatase TiO_2 Photocatalyst Induced by Atomic Hydrogen-Occupied Oxygen Vacancies. *Adv. Mater.* **2018**, *30*, 1704479. [CrossRef] [PubMed]
28. Wan, N.; Xing, Z.; Kuang, J.; Li, Z.; Yin, J.; Zhu, Q.; Zhou, W. Oxygen Vacancy-Mediated Efficient Electron-Hole Separation for C-N-S-Tridoped Single Crystal Black TiO_2(B) Nanorods as Visible-Light-Driven Photocatalysts. *Appl. Surf. Sci.* **2018**, *457*, 287–294. [CrossRef]
29. Huang, L.; Duan, Z.; Song, Y.; Li, Q.; Chen, L. $BiVO_4$ Microplates with Oxygen Vacancies Decorated with Metallic Cu and Bi Nanoparticles for CO_2 Photoreduction. *ACS Appl. Nano Mater.* **2021**, *4*, 3576–3585. [CrossRef]
30. Vu, M.-H.; Quach, T.-A.; Do, T.-O. The Construction of Ru-doped In_2O_3 Hollow Peanut-like Structure for An Enhanced Photocatalytic Nitrogen Reduction under Solar Light Irradiation. *Sustain. Energ. Fuels* **2021**, *5*, 2528–2536. [CrossRef]
31. Wang, J.; Su, J.; Chen, H.; Zou, X.; Li, G. Oxygen Vacancy-rich, Ru-doped In_2O_3 Ultrathin Nanosheets for Efficient Detection of Xylene at Low Temperature. *J. Mater. Chem. C* **2018**, *5*, 2528–2536. [CrossRef]
32. Wu, Q.; Shen, C.; Rui, N.; Sun, K.; Liy, C. Experimental and Theoretical Studies of CO_2 Hydrogenation to Methanol on Ru/In_2O_3. *J. CO_2 Util.* **2021**, *53*, 101720. [CrossRef]
33. Li, H.; Tang, X.; Zhong, J.; Li, J.; Chen, G.; Chen, C. Carbon Nanofibers Induced Tunable Oxygen Vacancies on BiOCl for High Efficient Destruction of Decontaminants. *Surf. Interfaces* **2021**, *25*, 101247. [CrossRef]
34. Huang, J.; Dou, L.; Li, J.; Zhong, J.; Li, M.; Wang, T. Excellent Visible Light Responsive Photocatalytic Behavior of N-Doped TiO_2 toward Decontamination of Organic Pollutants. *J. Hazard. Mater.* **2021**, *403*, 123857. [CrossRef]
35. Zhang, J.; Balasubramanian, R.; Yang, X. Novel 3D Multi-Layered Carbon Nitride/Indium Sulfide Heterostructure for Boosted Superoxide Anion Radical Generation and Enhanced Photocatalysis under Visible Light. *Chem. Eng. J.* **2023**, *453*, 139776. [CrossRef]
36. Wang, W.; Chen, X.; Liu, G.; Shen, Z.; Xia, D.; Wong, P.K.; Yu, J.C. Monoclinic Dibismuth Tetraoxide: A New Visible-Light-Driven Photocatalyst for Environmental Remediation. *Appl. Catal. B Environ.* **2015**, *106–177*, 444–453. [CrossRef]
37. Huang, Y.; Wang, K.; Guo, T.; Li, J.; Wu, X.; Zhang, G. Construction of 2D/2D Bi_2Se_3/g-C_3N_4 Nanocomposite with High Interfacial Charge Separation and Photo-Heat Conversion Efficiency for Selective Photocatalytic CO_2 Reduction. *Appl. Catal. B Environ.* **2020**, *277*, 119232. [CrossRef]
38. Chang, W.-C.; Kuo, C.-H.; Juan, C.-C.; Lee, P.-J.; Chueh, Y.-L.; Lin, S.-J. Sn-Doped In_2O_3 Nanowires: Enhancement of Electrical Field Emission by a Selective Area Growth. *Nanoscale Res. Lett.* **2012**, *7*, 684. [CrossRef]
39. He, L.; Wood, T.E.; Wu, B.; Dong, Y.; Hoch, L.B.; Reyes, L.M.; Wang, D.; Kubel, C.; Qian, C.; Jia, J.; et al. Spatial Separation of Charge Carriers in $In_2O_{3-x}(OH)_y$ Nanocrystal Superstructures for Enhanced Gas-Phase Photocatalytic Activity. *ACS Nano* **2016**, *10*, 5578–5586. [CrossRef]

40. Lv, Y.; Cao, X.; Jiang, H.; Song, W.; Chen, C.; Zhao, J. Rapid Photocatalytic Debromination on TiO_2 with In-situ Formed Copper Co-catalyst: Enhanced Adsorption and Visible Light Activity. *Appl. Catal. B Environ.* **2016**, *194*, 150–156. [CrossRef]
41. Wan, Z.; Mao, Q.; Chen, Q. Proton-dependent Photocatalytic Dehalogenation Activities Caused by Oxygen Vacancies of In_2O_3. *Chem. Eng. J.* **2021**, *403*, 126389. [CrossRef]
42. Sun, C.; Chen, C.; Ma, W.; Zhao, J. Photocatalytic Debromination of Decabromodiphenyl Ether by Graphitic Carbon Nitride. *Sci. China Chem.* **2012**, *55*, 2532–2536. [CrossRef]